PHYSICAL REVIEW APPLIED **24,** 044047 (2025)

Two-dimensional functionalized Mo_2NT_2 ($T = H, O$) monolayer as promising candidates for NO_x gas capture agents and sensors

Zebang Cheng,[1] Yiran Ying,[2] Yamin Xue,[1] Ben Wang,[1] Ziqiu Wang,[1] Lin Peng,[1,*] Tingting Shi,[3]
Jing Chen,[1] Xiaolin Liu,[1] Haitao Huang,[2,†] and Jia Lin[1,‡]

[1] *Department of Physics, Shanghai University of Electric Power, Shanghai 200090, China*
[2] *Department of Applied Physics and Research Institute for Smart Energy, The Hong Kong Polytechnic University, Hong Kong 999077, China*
[3] *Department of Physics, Jinan University, Guangzhou 510632, China*

(Received 13 February 2025; revised 29 June 2025; accepted 12 September 2025; published 16 October 2025)

This study employs first-principles calculations to investigate functionalized Mo_2NT_2 ($T = Ø$, H, O, F) MXenes as dual-functional materials for toxic gas capture and sensing applications. The surface of the pristine Mo_2N surface is unsaturated, possesses dangling bonds, and exhibits a strong capability to capture various environmental gases. Surface functionalization significantly modulates this behavior: Mo_2NH_2 demonstrates remarkable selectivity toward NO_x capture, while Mo_2NO_2 emerges as a superior NO sensor due to its optimal adsorption strength (−0.342 eV), substantial charge transfer (−0.197 *e*), and 14%–18% current reduction in nanodevice measurements. Notably, investigations of mixed-terminated $Mo_2NO_x(OH)y$ systems reveal that hydroxyl concentration dictates NO reaction pathways: low OH triggers proton abstraction, forming O-N-H structures, whereas high OH induces direct O-H cleavage, generating H_2N-OH. Although water passivation mitigates these reactions, irreversible chemical transformations persist, underscoring that precise control of surface chemistry, particularly terminal-group engineering, is essential for achieving the selective capture capabilities and reversible sensing performance required for next-generation MXene-based gas management platforms.

DOI: 10.1103/jst3-45bj

I. INTRODUCTION

Gas sensor advancement is essential for detecting toxic industrial gases, monitoring environmental pollution, and creating sustainable energy solutions [1–4]. In the past half century, semiconductor materials have been commercially used to create gas sensors on the market [5] due to their affordability and quick response times [6]. However, they exhibit a high operating temperature, low conductivity, and restricted sensitivity. Gas sensors with exceptional sensitivity are necessary for diagnosing serious diseases, environmental monitoring, and military surveillance [7,8]. Therefore, the development of gas sensors with rapid and efficient detection capabilities for low gas concentrations is of great significance [9,10]. In 2007, Liang *et al.* applied graphene-based microsized sensors to detect gases such as NO_2, NH_3, H_2O, and CO at concentrations of 1-ppb levels [11]. The sensors were able to detect individual adsorbed molecules by monitoring changes in the local carrier concentration within graphene. Similar to solid-state sensors, the adsorption of gas molecules on the graphene surface achieves gas detection by acting as a donor or receptor molecule and influencing variations in conductivity on the graphene surface [11]. Although graphene has attracted considerable attention, its simple chemical properties limit its application [12].

MXenes are emerging two-dimensional materials like graphene, consisting of transition metals, carbides, and nitrides. They form an atomic sheet with strongly bonded atoms by etching the max phase, i.e., $M_{n+1}AX_n$, where M is a transition-metal element, A is a group IIIA or IVA metal element, and X is carbon or nitrogen [12–14]. The atomic sheets are linked by weak interlayer van der Waals interactions [15]. Pristine MXenes have electron unsaturation, which results in their surfaces being terminated by functional groups like F, O, or OH during liquid etching [16]. This alters their physical and chemical properties, making them suitable for applications such as energy storage [17], catalysis [18], and gas sensors [19]. MXenes are promising candidates for the next generation of gas detectors because of their high conductivity, low noise, vast surface area, high volume ratio, and customizable surface termination groups [12].

---

[*] Contact author: plpeng@shiep.edu.cn
[†] Contact author: aphhuang@polyu.edu.hk
[‡] Contact author: jlin@shiep.edu.cn

Lee *et al*. synthesized two-dimensional $Ti_3C_2T_x$ material as a flexible sensor and successfully detected ethanol, methanol, acetone, and ammonia at room temperature. The detection limit of acetone gas was calculated to be 9.27 ppm [19]. It was proposed by Khakbaz *et al*. that the interaction between NH_3 gas molecules and $Ti_3C_2T_x$ substrates with low end ratios on the fluorine surface was stronger. The calculated charge-transfer amount of NH_3 to the modulation terminal is -0.098 *e*, and the adsorption energy is -0.36 eV [20]. Xiao *et al*. researched the interaction between ammonia in various charge states and functionalized M_2CO_2 ($M =$ Sc, Ti, Zr, and Hf), proposing that the O-end semiconductor MXenes could serve as a material for NH_3 sensors [21]. By calculating the electronic properties of materials and the transport behavior of devices, Naqvi proposed that S-functionalized M_2N ($M =$ Ti, V) could serve as an excellent sensing material for NO and NO_2 [22]. Shukla *et al*. suggested that two-dimensional materials with moderate adsorption energy, high charge-transfer capacity, and short recovery times could be potential gas sensors. For instance, functionalized $2H$-Mo_2BH_2 has been identified as a promising NH_3 sensor [23]. These studies illustrate the potential of MXene materials, especially functionalized MXenes, in the gas sensor sector.

Nevertheless, despite significant research efforts on MXene for gas sensing, challenges remain in achieving superior selectivity and shorter recovery times [12]. This motivates our exploration of alternative two-dimensional MXene materials and the modulation of their gas-sensitive properties through surface-functionalization techniques. Research reports indicate that Mo_2NT_2 materials can be synthesized through the ammonization of Mo_2CT_2 at elevated temperatures (up to 600 °C for 1 h) [24]. Furthermore, two-dimensional monolayer Mo_2N demonstrates potential as an anode material for lithium-ion batteries. This potential arises from its high specific charge capacity ($\sim$520 mA h g^{-1}) and its enhanced electronic conductivity following Li-atom adsorption [25]. Building on these findings, we investigate whether Mo_2NT_2 exhibits a significant modulation of its electronic conductivity upon adsorption of specific gases. This property is a critical characteristic for potential application as a sensitive material in resistive gas sensors.

Therefore, we comprehensively evaluated the gas-sensing potential of monolayer Mo_2N and its surface termination groups (H, F, O) by analyzing charge transfer, differential charge density, projected density of states (PDOS), thermal stability, and electronic transport behavior. It is proposed that Mo_2N and Mo_2NH_2 can be used as capture agents for NO_x toxic gases, and Mo_2NO_2 is identified as a potential reversible sensing material for NO detection. The distinct adsorption behaviors of NO on pristine monolayer Mo_2N and functionalized Mo_2NT_2 ($T =$ H, O, F) are explained. We anticipate that this study will provide pivotal guidance for the development of high-efficiency toxic-gas-selective capture agents and advanced gas sensor materials.

II. COMPUTATIONAL METHODS

All simulations employed first-principles methods via the Vienna *ab initio* simulation package [26,27]. Electron-ion interactions were modeled using the projector augmented-wave pseudopotential framework. For charge-exchange interactions, the Perdew-Burke-Ernzerhof (PBE) functional within the generalized gradient approximation [28] served as the primary computational approach. To achieve quantitatively accurate band gaps and electronic structures, we supplemented the study with the screened hybrid HSE06 functional [29], which incorporated 25% exact Hartree-Fock exchange and a screening parameter of 0.2 $Å^{-1}$. According to the expansion of the electron wave function, the cutoff value of the plane-wave energy with 520 eV is selected, and the vacuum layer spacing is set to 20 Å to avoid periodic boundary impact. The Brillouin zone is modeled using a $12 \times 12 \times 1$ Monkhorst-Pack k-point grid scheme, and the conjugate gradient algorithm is employed to relax the unit-cell vector of lattice parameters and atomic coordinates. The relaxation process continues until the residual force on each atom is below 0.01 eV/Å and the energy difference between electronic steps is less than 10^{-5} eV to avoid residual stress. The 3×3 supercells of Mo_2N and functionalized MXenes are denoted as X0, X1, X2, and X3 substrates. The Brillouin zone adopts a $4 \times 4 \times 1$ Monkhorst-Pack k-point grid for structural relaxation and self-consistent calculations. We used density-functional perturbation theory to calculate the phonon-band structure, and the system was coupled to the Nosé-Hoover thermostat for *ab initio* molecular dynamics (AIMD) simulations that lasted for 10 ps in the *NVT* ensemble. We added the DFT-D3 van der Waals correction using Grimme's semiempirical dispersion-correction method in all calculations to consider the long-term correlation effect [30]. Chemical bond analysis adopts the crystal orbital Hamilton population (COHP) method, which is implemented in the local orbital basis suite towards electronic structure reconstruction code [31].

The formation energy, E_{form}, of functional groups on MXenes is defined as

$$E_{\mathrm{form}} = E_{\mathrm{Mo_2N}T_2} - E_{\mathrm{Mo_2N}} - E_{T_2}, \tag{1}$$

where $E_{\mathrm{Mo_2N}T_2}$, $E_{\mathrm{Mo_2N}}$, and E_{T_2} represent the total energy of functionalized Mo_2NT_2 ($T =$ H, O, F); the total energy of the original material; and the total energy of group gas-phase H_2, F_2, and O_2, respectively.

The adsorption energy of the system is defined as

$$E_{\mathrm{ads}} = E_{\mathrm{Mo_2N}T_2+\mathrm{gas}} - E_{\mathrm{Mo_2N}T_2} - E_{\mathrm{gas}}, \tag{2}$$

where $E_{\mathrm{Mo_2N}T_2+\mathrm{gas}}$, $E_{\mathrm{Mo_2N}T_2}$, and E_{gas} represent the total energy of the monolayer and adsorbed gas, the total energy of the monolayer substrate, and the total energy of isolated gas molecules, respectively.

Recovery time is an important index of the gas sensor. Based on transition-state theory, it has an exponential relationship with the adsorption energy, as follows [32]:

$$\tau = \upsilon_0^{-1} e^{-E_{\mathrm{ads}}/k_{\mathrm{B}}T}, \tag{3}$$

where T is the temperature, k_{B} is the Boltzmann constant (8.62×10^{-5}), and υ_0 is the trial frequency (10^{12}). We can get the recovery time of the system at different temperatures through this formula.

III. RESULTS AND DISCUSSION

A. Structural and electronic properties of Mo_2N

In this section, we investigate the structural and electronic properties of Mo_2N. The space-group number of the isolated single-layer Mo_2N structure is 164. Single-layer Mo_2N after relaxation optimization is shown in Fig. 1(a), and its lattice structural parameters are $a = b = 2.810$ Å, which are very close to experimental reports [24]. The calculated bond lengths of its neighboring Mo and N atoms are 2.130 Å. To evaluate its stability, we perform phonon-dispersion spectroscopy calculations and AIMD simulations. Figure 1(b) shows the phonon spectrum with missing imaginary frequencies, which indicates that the structure is stable [33]. In addition, 10-ps AIMD simulations are conducted on the Mo_2N system to verify the thermodynamic stability at three different temperatures (300, 500, and 700 K), as shown in Fig. S1(a)–S1(c) within the Supplemental Material [34]. Although single-layer Mo_2N exhibits atomic vibrations at high temperatures, its energy fluctuates around the average value. The material's framework remains stable without appreciable deformation for durations below 10 ps. Thermal-vibration-induced atomic displacement does not inherently indicate material instability, and the displacements are inherent reactions of the system to the thermodynamic conditions. Monolayer Mo_2N can maintain stability, even at elevated temperatures. Figure 1(c) illustrates that the energy band of Mo_2N extends beyond the Fermi level. And the SOC can open degeneracy at the Γ point while having little effect on the energy-band structure. Therefore, SOC is not considered in subsequent calculations.

B. Structure and stability of Mo_2NT_2

Modifying the terminal group on the surface of MXenes can alter their chemical characteristics. The surface of single-layer Mo_2N is unsaturated, leading to the unavoidable presence of termination groups on its surface. This section analyzes Mo_2NT_2 ($T =$ H, O, F) functionalized with various groups. The positions of termination groups in uncovered MXenes are influenced by the variance in electronegativity between metal cations and anions. We used Mo_2N with two functional groups arranged in a 1 × 1 configuration on opposite sides of Mo_2N to create the Mo_2NT_2 structure. Combining the symmetry of Mo_2N precursor cells, two different (ST1 and ST2) double-sided adsorption sites are considered for different termination groups, as depicted in Figs. 2(a) and 2(b), and the corresponding formation energies of the two structures have been computed and are presented in Fig. 2(c). In the ST1 configuration, the T atom is arranged vertically with Mo atoms on both sides. And in the ST2 configuration, T atoms are arranged vertically on both sides of N atoms. The lowest formation energies of Mo_2NH_2, Mo_2NF_2, and Mo_2NO_2 are −0.781, −6.634, and −8.339 eV, respectively. Additionally, phonon-dispersion calculations on these three lowest-energy configurations demonstrated their dynamic stability (Fig. S2 within the Supplemental Material [34]). This indicates that the functionalization of Mo_2N was feasible. Furthermore, the integrated crystal orbital Hamilton

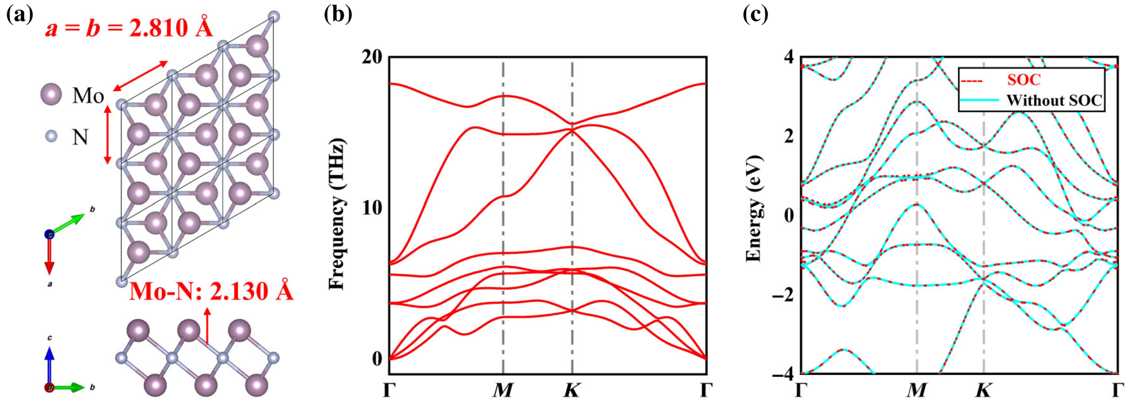

FIG. 1. (a) Top and side views of the Mo_2N monolayer. (b) Phonon dispersion spectrum of the Mo_2N monolayer. (c) Band structures of Mo_2N with and without considering the spin-orbit-coupling (SOC) effect.

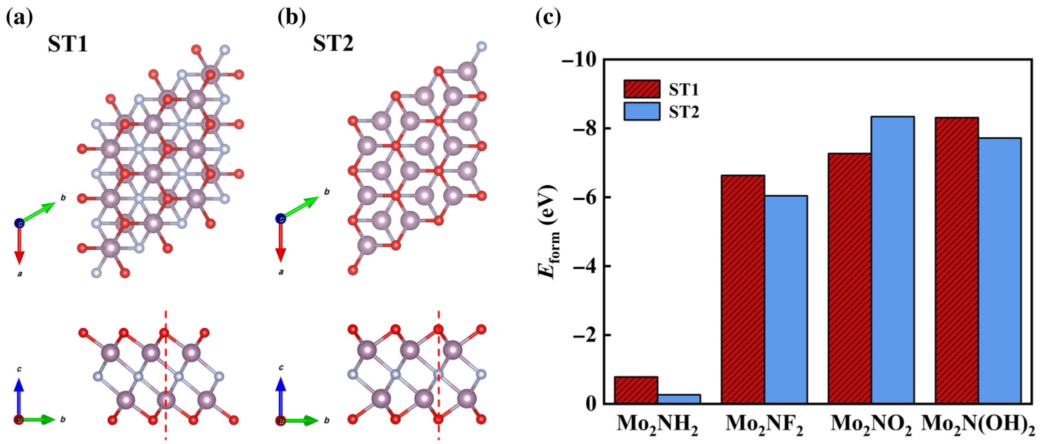

FIG. 2. Top and side views of (a) ST1 and (b) ST2, two different functionalized structures for single-layer Mo_2N. (c) Formation energies (eV) of two structures calculated for three functionalized Mo_2NT_2.

population (ICOHP) is calculated to obtain a quantitative description of the Mo—T bond strength (Fig. 3). A larger absolute value of ICOHP indicates a stronger bond energy. The ICOHP values between H-Mo, F-Mo, and O-Mo are −0.99, −1.16, and −2.83, respectively, with bond lengths of 1.98, 2.21, and 2.03 Å, which are consistent with the bonding strength. Meanwhile, AIMD simulations (Fig. S1 within the Supplemental Material [34]) for 10 ps at 300, 500, and 700 K were performed on the most stable configuration of functionalized MXenes. The energy curve generated by AIMD shows vibrations close to the mean value, meaning that the three functionalized MXenes remain stable across various temperatures (300, 500, and 700 K). These findings further demonstrate the potential use of the functionalized Mo_2N sensor from room temperature to high temperatures.

C. Electronic structure and properties of Mo_2NT_2 ($T = $ H, O, F)

As illustrated in Fig. 4(a), the PDOS of Mo_2N reveals a pronounced hybridization peak centered at −6 eV between Mo *d* and N *p* orbitals, exhibiting a broad spectral overlap that indicates strong covalent Mo—N bonding. Crucially, within the Fermi window (−3–3 eV), the persistent *d*-*p* orbital hybridization results in substantial band overlap, leading to vanishing band gaps and metallic behavior. While hybrid HSE06 calculations were performed for comparison [Fig. 4(b)], the quantitative agreement in hybridization features and metallicity confirm that PBE reliably captures the essential electronic characteristics of Mo_2N systems without overestimating metallic traits. Consequently, subsequent analyses are based on PBE calculations. Mechanistically, charge transport is primarily

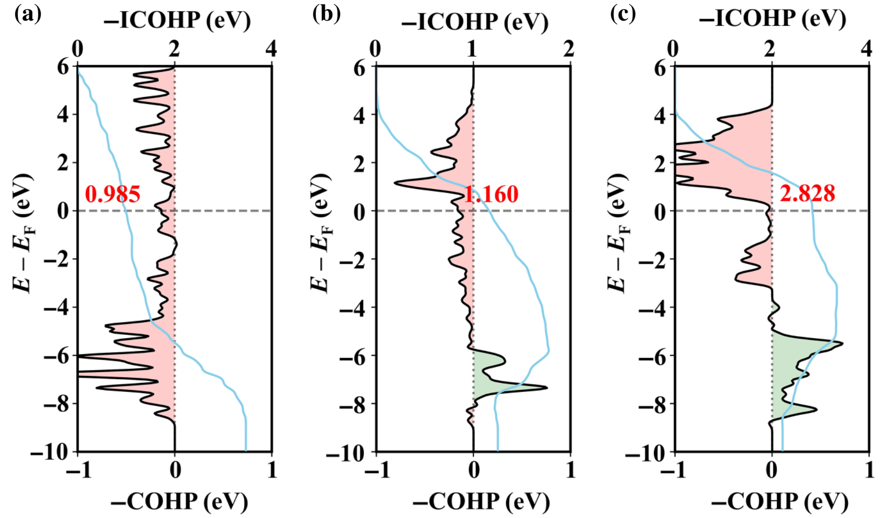

FIG. 3. Average −COHPs and −ICOHPs of (a) H—Mo, (b) F—Mo, and (c) O—Mo bonds. Green area represents the bonding contribution, and red area represents the antibonding contribution. Blue curve represents the integral of −ICOHPs; −ICOHP integral value is indicated in red font; and gray dotted line represents Fermi energy level.

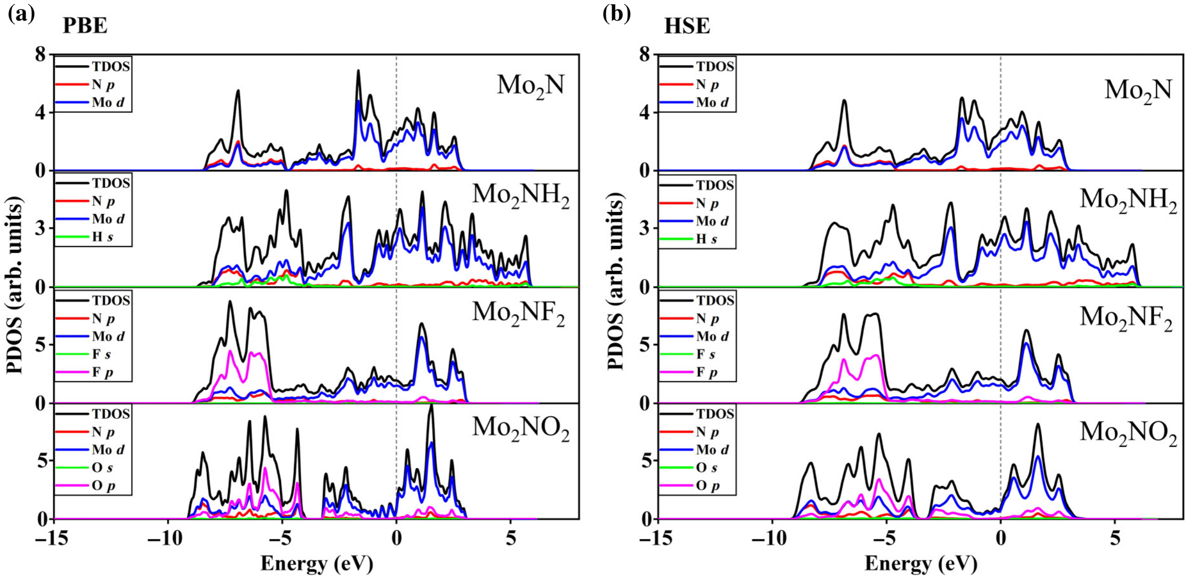

FIG. 4. Total DOS (TDOS) and PDOS of monolayered Mo_2N, Mo_2NH_2, Mo_2NF_2, and Mo_2NO_2. (a) PBE calculations. (b) HSE06 calculations.

governed by the Mo *d* orbitals, which dominate the DOS near E_F, whereas N *p* orbitals facilitate conductivity through covalent-channel mediation.

In addition, the PDOS of Mo_2NT_2 is calculated to gain a deeper understanding of its electronic properties, as shown in Fig. 4. In Mo_2N, the conduction band and valence band are created through the hybridization of Mo *d* and N *p* orbitals. The primary contribution comes from the nonbonding orbitals of Mo *d*, representing the presence of dangling bonds on the surface of Mo. The bands are divided by a narrow band gap, ranging from −4.8 to −4.7 eV below the Fermi level, without impacting the metallic characteristics. The nonbonding-orbital contribution of Mo *d* decreases in Mo_2NF_2 and Mo_2NO_2, leading to a change of the PDOS curve around the Fermi level and a pseudogap towards negative energy. The pseudogap lies between the bonding orbitals at negative energies and the nonbonding orbitals at positive energies. Its width expands, meaning an increase in the covalent bond's strength and the structure's stability. The valence band of functionalized Mo_2NT_2 ($T = $ H, O, F) ranges from −4 to −8 eV and is mostly formed through Mo *d*-N *p* and Mo *d*-*T* *s* or *p* orbital hybridization. Between 0 and 4 eV, it consists primarily of Mo *d* and *T* *p*. The *T* *s*(*p*) state makes a minor contribution to the conduction band. Interestingly, after the O group is terminated, a new energy band develops below the Fermi energy (−3.9 to −3.2 eV) due to hybridization of the O *p* and *M* *d* orbitals. This reveals the possibility of transforming it into a semiconductor material through band-gap engineering.

D. Gas adsorption on MXenes

The four adsorption sites for a gas, as shown in Fig. 5, are considered to obtain the gas-adsorption energies of substrates X0–X3. To quantify the strength of the interaction between gas molecules and MXenes, Bader charge transfer (C_T) and the closest distance between gas molecules and substrate were calculated, as shown in Tables S1–S3 within the Supplemental Material [34] and Table I.

The most stable configuration of gas molecules on the X0 substrate is described in Fig. S3 within the Supplemental Material [34]. As shown in Table I, in all scenarios, the X0 substrate loses electrons, and all adsorption processes are exothermic reactions. The X0 substrate exhibits the highest adsorption energy for NO ($E_{ads} = -4.218$ eV). It also has the lowest adsorption energy for CH_4 ($E_{ads} = -0.339$ eV) but a relatively high charge transfer (1.032 *e*). It is necessary to point out that H_2S is cracked in different orientations of monolayer Mo_2N in Fig. S4 within the Supplemental Material [34], which is similar to the cracking of H_2S on the metal surface reported in previous studies [35,36]. Nevertheless, it is beyond the scope of the current work, so it is not discussed here.

Figure 6 depicts the isosurface of total charge density for monolayer Mo_2N adsorbed with gas molecules, visualizing interactions between pristine Mo_2N and adsorbates. To gain deeper insights into charge-transfer mechanisms, the differential charge density ($\Delta\rho$) was calculated based on the following definition:

$$\Delta\rho = \rho_{\text{adsorbate}} - \rho_{\text{MXene}} - \rho_{\text{gas}} \quad (4)$$

where $\rho_{\text{adsorbate}}$ is the self-consistent charge density of the adsorbed system (gas molecule on MXene), ρ_{MXene} denotes the self-consistent charge density of the isolated MXene substrate at the same atomic positions as in the

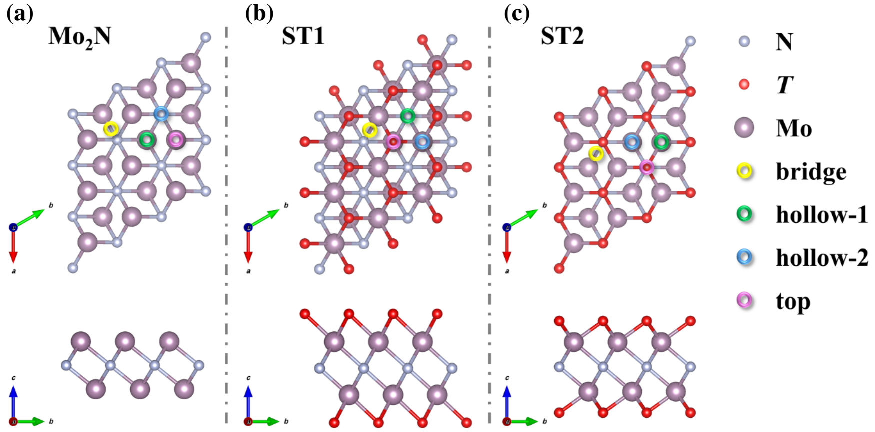

FIG. 5. Adsorption sites on (a) Mo_2N, (b) ST1, (c) ST2 surfaces. Gold, bridge site; green, hollow-1 site; blue, hollow-2 site; lavender, top site. Bridge, hollow, and top sites represent the gap positions between two Mo terminal groups, directly above the Mo terminal group, and between the three Mo terminal groups.

adsorbed system, and ρ_{gas} represents the self-consistent charge density of the isolated gas molecule in its adsorbed configuration.

The Mo site is a charge-depletion region that forms a charge-accumulation region with the central atom or hydrogen atom of the interacting gas molecule. The adsorbed gas acts as a Lewis base with lone-electron pairs, and it strongly interacts with the surface of the X0 substrate. The interaction between the HOMO of gas molecules and the unoccupied crystal orbitals of the substrate reduces the energy states, resulting in a transfer of partial charge from the Lewis base to the Lewis acid, thereby forming new bonds [37]. The PDOS of the X0 substrate and gas-adsorption systems support this point (Fig. S5 within the Supplemental Material [34]). During the adsorption of CH_4, NH_3, NO_2, SO_2, CO, and CO_2, Mo *d* and C, O, N, or S *p* orbitals are hybridized at 0–5 eV in the conduction band. The conduction band of the substrate is mainly contributed to by Mo *d* nonbonding orbitals. When the adsorbed gas is close to the substrate surface, additional electrons will be introduced into the unoccupied orbitals of Mo *d* on the substrate surface. This means that the valence-layer electrons of Mo interact with the valence-layer electrons of the adsorbed gas and further affect the DOS at the Fermi level. For example, NH_3 donates its lone pair to the surface, where hybridization occurs between the N *p* orbital of NH_3 and the Mo *d* orbital. This bonding mechanism is further supported by distinct resonance peaks of the Mo *d* and N *p* DOS within the energy range of −10 to −3 eV, as evidenced by Fig. S5(b) within the Supplemental Material [34].

TABLE I. Adsorption energy of gas molecules adsorbed on X0 substrate; H_2S and NO_2 gas adsorbed on X1 substrate; NO gas adsorbed on X1, X2, or X3 substrates; C_T; and distance from substrates.

Substrates/gas molecules	E_{ads} (eV)	C_T (e)	$d_{\text{gas - Mo}_2\text{N}}$ (Å)
Mo_2N/CH_4	−0.339	1.032	2.078
Mo_2N/NO	−4.218	1.667	1.27
Mo_2N/H_2S	−1.809	0.382	1.94
Mo_2N/CO_2	−1.672	2.055	1.54
Mo_2N/NO_2	−3.589	1.372	2.02
Mo_2N/SO_2	−3.074	1.433	2.04
Mo_2N/CO	−2.415	0.808	1.97
Mo_2N/NH_3	−1.532	0.631	2.34
Mo_2NH_2/H_2S	−0.357	−0.104	2.23
Mo_2NH_2/NO_2	−1.624	0.045	1.032
Mo_2NH_2/NO	−3.208	0.572	1.591
Mo_2NF_2/NO	−0.368	−0.209	2.272
Mo_2NO_2/NO	−0.342	−0.197	1.966

E. NO gas adsorption on Mo_2NT_2 (T = H, F, O)

Based on the most stable adsorption configurations of gas molecules on X1, X2, and X3 substrates considered here (Figs. S6–S8 within the Supplemental Material [34]), termination groups have a significant impact on the gas sensitivity of pristine Mo_2N. The front and side views of the most stable arrangement of NO adsorbed on the surface of X0–X3 substrates are exhibited in Figs. 7(a)–7(d), respectively. The curves in the figures represent the average potential diagram of the adsorption systems. In the X0 substrate, Mo_2N has a significant adsorption reaction with NO, and the Mo—N bond of the substrate increases from 2.12 to 2.19 Å. In the X1 substrate, the Mo atom close to the NO gas molecule is pulled out of the layer, and the corresponding Mo—N bond increases from 2.12 to 2.97 Å. There is only a slight alteration in the Mo—N bond in X2 and X3. The plane average potential curve of the system could more clearly describe the energy distribution at the interface of the adsorption system. The left platform represents the vacuum level of the Mo(T)-

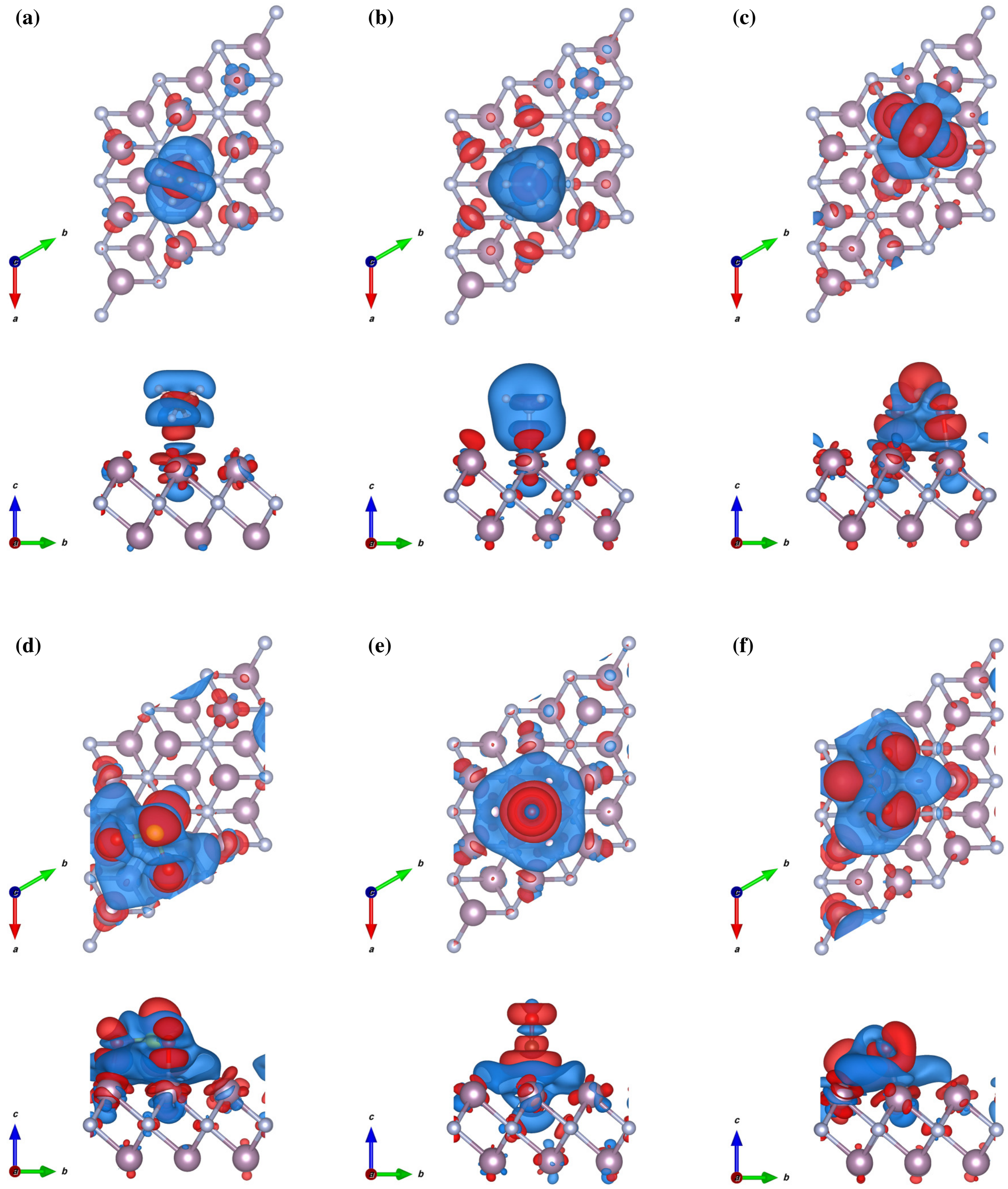

FIG. 6. Order of the differential charge diagram is (a) CH_4, (b) NH_3, (c) NO_2, (d) SO_2, (e) CO, and (f) CO_2. It corresponds to the order of (a)–(c), (e)–(g) in Fig. S3 within the Supplemental Material [34]. Red and blue correspond to the charge-accumulation area and charge-consumption area, respectively. Isosurface of each image is set to 0.001 $e/\text{Å}^3$.

(H, F, O) terminated surface of the original substrate, and the right platform represents the vacuum level of the NO-terminated surface. There is a step in the vacuum region. After the adsorption of NO gas, charge transfer occurs on the substrate surface, which leads to the generation of an induced dipole and an increase in the dipole moment, leading to further polarization. Thus, there is a potential shift at the interface, which affects the work function (W_F). W_F is defined as the difference between the vacuum level (E_{vac}) and the Fermi level (E_{F}), i.e., $W_F = E_{\text{vac}} - E_{\text{F}}$. It represents the minimum energy required for an electron to transition from the interior of a material to the vacuum level. Any alteration in W_F will impact the conductivity of the system, which is directly linked to the sensing capabilities of the adsorption surface. When NO gas molecules are adsorbed on substrates, the changes in

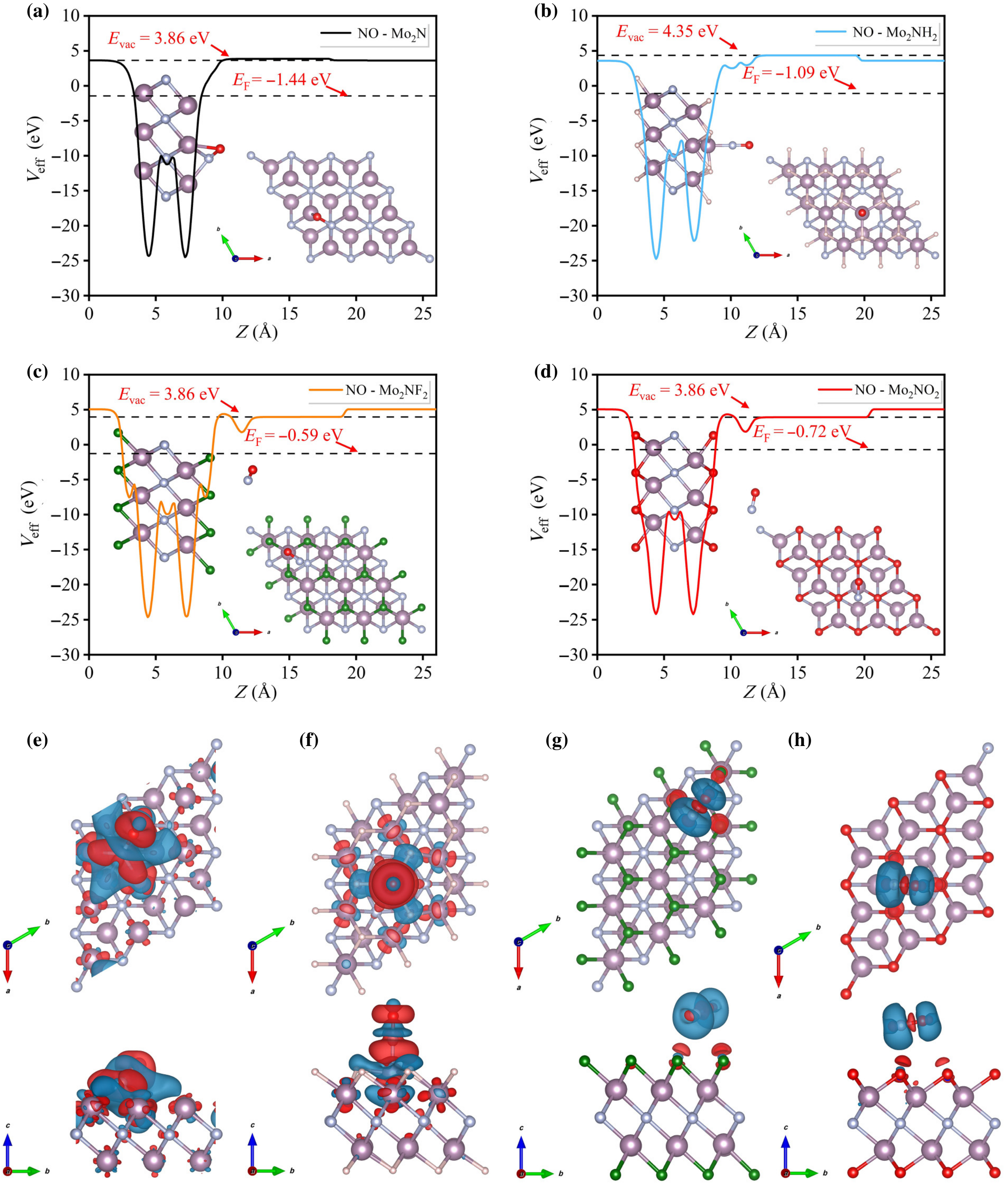

FIG. 7. Average curve of the electrostatic potential on the plane perpendicular to the substrate surface and NO adsorbed on (a) Mo_2N, (b) Mo_2NH_2, (c) Mo_2NF_2, and (d) Mo_2NO_2 substrates. E_{vac} represents the vacuum level of the adsorption surface and E_F represents the Fermi level of the adsorption system. Charge-density difference diagrams of (e) NO/Mo_2N, (f) NO/Mo_2NH_2, (g) NO/Mo_2NF_2, and (h) NO/Mo_2NO_2, where the reference charge density is 0.001 e/Å^3; blue represents the charge-depletion region, and red represents the charge-accumulation region.

W_F values are 0.25, 0.75, −1.08, and −1.14 eV. W_F of X0 and X1 substrates increase significantly, likely due to the adsorption of gases that cause slight deformation of the substrate while also acting as oxidants to remove charges from the substrate. The significant reduction of W_F in X2 and X3 substrates may be attributed to NO gas providing

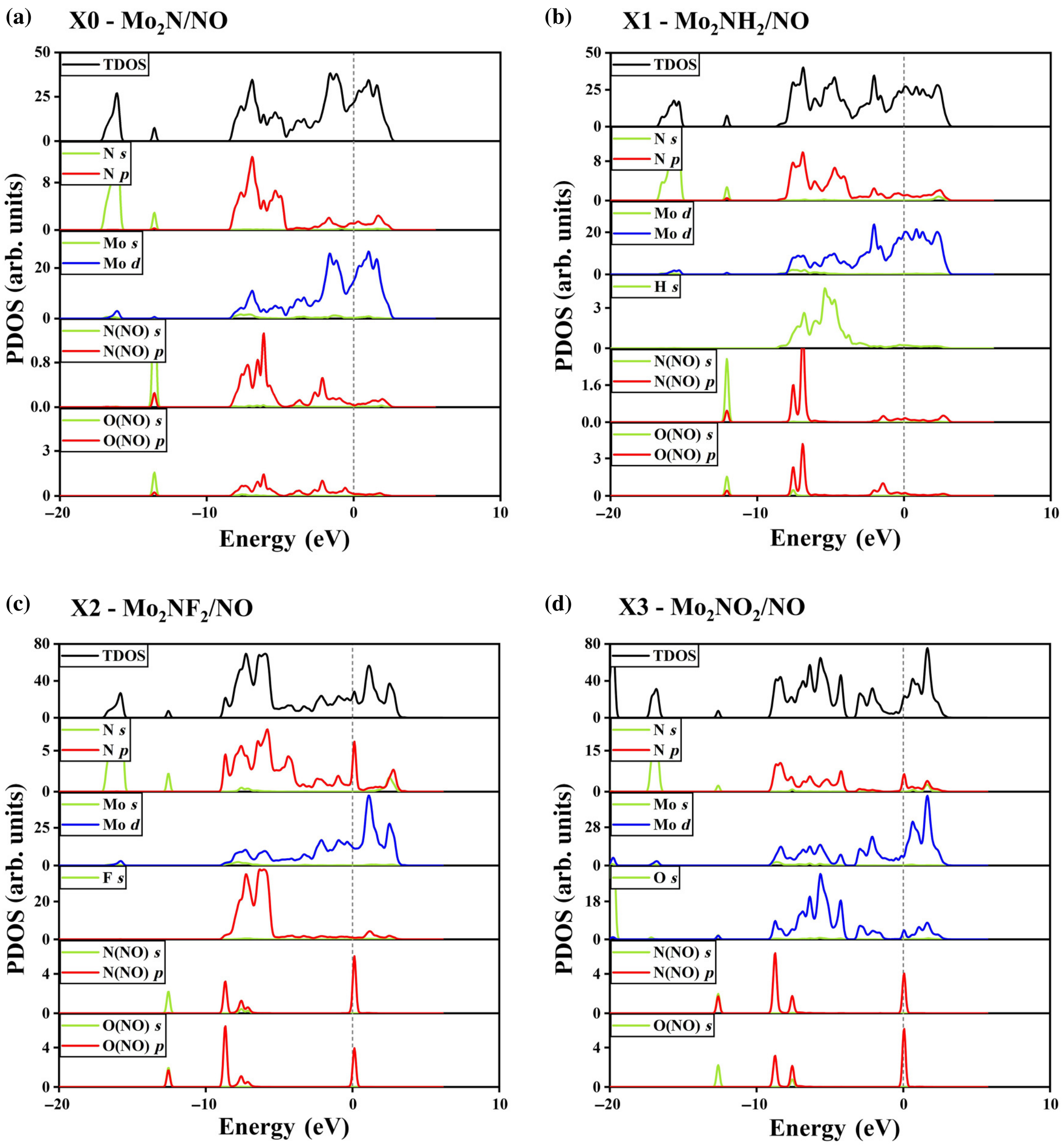

FIG. 8. DOS and PDOS for NO/Mo_2NT_2 ($T = \emptyset$, H, F, O) system are calculated as follows: (a) NO/Mo_2N, (b) NO/Mo_2NH_2, (c) NO/Mo_2NF_2, and (d) NO/Mo_2NO_2. Fermi level is taken to be zero and displayed with a black dashed line.

additional electrons to the substrate. The alteration in W_F is essential for NO gas detection, as it directly modulates interfacial charge transfer and carrier concentration, thereby governing conductivity changes that underpin the fundamental mechanism of resistive gas sensing.

We further investigated the PDOS of the NO/Mo_2NT_2 ($T = \emptyset$, H, F, O) adsorption systems to elucidate their electronic properties. As depicted in Figs. 8(a)–8(d), distinct orbital resonance peaks in the DOS are observed between the O *s* and N *p* orbitals of the adsorbed NO molecule and the Mo *d* orbitals within the energy range of −8 to 2 eV in the X0 system. This clearly indicates the formation of covalent bonds between the N and O atoms of NO and the surface Mo atoms, which is fully consistent with the corresponding atomic configuration shown in Fig. 7(a). For the X1 system, a comprehensive comparison of the DOS [Fig. 8(b)] and the atomic structure [Fig. 7(b)] reveals a subtle orbital energy overlap between the N *p* orbital of NO and Mo *d* orbitals around −8 to −6 eV, confirming covalent bonding between the N atom of NO and the surface Mo. Similar characteristic DOS peaks associated with the O *p* orbitals reflect the intrinsic N—O bond within the adsorbed NO molecule. In the X2 and X3 adsorption systems, significant DOS peaks emerge at the Fermi level for the N *p* and O *p* orbitals of NO. This phenomenon is attributed to charge transfer from the MXene surface to the

N and O atoms of NO, as evidenced by the charge-density difference plots presented in Figs. 7(g) and 7(h). Consequently, electron depletion occurs in the antibonding π^* orbitals of NO, thereby strengthening the N—O bond. The presence of pronounced red charge-accumulation regions between the N and O atoms in Figs. 7(g) and 7(h) provides strong corroboration for this observation.

As illustrated in Fig. 9, Mo_2NF_2 and Mo_2NO_2 exhibit reversible NO-adsorption energies within the optimal sensing range of −0.3 to −0.6 eV, which are comparable to established NO-sensing materials, including Ti_2NS_2 [22], V_2NS_2 [22], CrP [38], $Ti_3C_2O_3$ [39] and phosphorene [40]. Notably, both materials demonstrate superior charge transfer relative to Ti_2NS_2, V_2NS_2, CrP, and phosphorene. These characteristics—moderate adsorption strength, facilitating desorption kinetics, coupled with enhanced charge transfer—signify significant electric field reconstruction at the gas-substrate interface. These synergistic characteristics highlight the promising potential of Mo_2NF_2 and Mo_2NO_2 as high-performance NO-sensing materials.

The recovery-time calculations based on transition-state theory [Eq. (3)] provide fundamental insights into the intrinsic desorption kinetics of NO from MXene surfaces, as show in Table II. For Mo_2NF_2 and Mo_2NO_2, the predicted recovery times range from milliseconds at 200 K to nanoseconds at 433 K, suggesting that thermal activation significantly enhances desorption rates.

In the context of surface physics and transition-state theory, the parameter v_0 represents the vibrational frequency of adsorbed NO molecules within the surface potential well, where 10^{12} Hz is commonly adopted as a reasonable approximation in solid-state systems. However, the actual desorption dynamics are influenced by two significant factors that deviate from ideal monolayer behavior. First, under low NO concentrations (at ppm levels), coverage-dependent effects become non-negligible, according to Langmuir adsorption theory, where the surface coverage shows a linear dependence on gas-phase pressure at low pressures, leading to faster recovery kinetics than that predicted by simple monolayer models. Second, real material surfaces invariably contain defects that can serve as deep trapping sites, substantially modifying the potential-energy landscape and creating additional binding states with higher activation barriers for desorption.

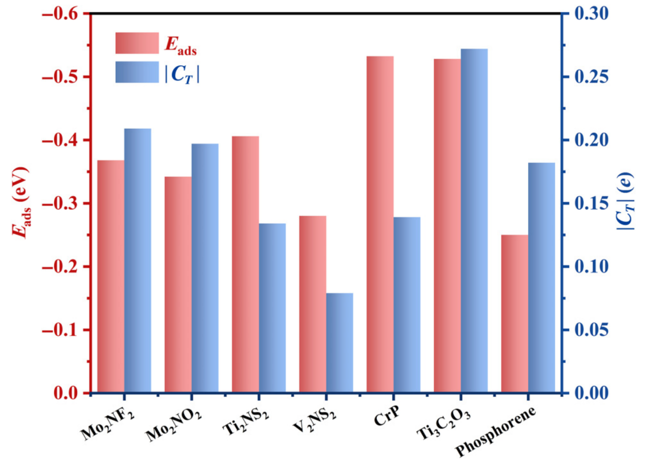

FIG. 9. Adsorption energies (E_{ads}) and absolute values of Bader charge transfer ($|C_T|$) for selected adsorbates on various two-dimensional materials.

While DFT calculations predict superior recovery performance compared to experimental systems (e.g., 24 s for NO_2 adsorption on $Pt/Cr\text{-}TiO_2/Pt$ at 200 K [41] or 94 s for H_2S adsorption on $ZnO/ZnCo_2O_4$ hollow tubes at 344 K [42]), this discrepancy stems from the inherent complexity of real-world devices. Practical systems typically involve polycrystalline materials with grain boundaries, which introduce structural disorder and localized strain, alongside additional rate-limiting steps, such as interfacial charge-transfer barriers and diffusion constraints—factors often underrepresented in idealized DFT simulations. Our results represent the theoretical limit for ideal single-crystal surfaces, establishing Mo_2NO_2 and Mo_2NF_2 as promising

TABLE II. Comparative analysis of NO-gas-sensing performance. Recovery time (τ) calculations for MXenes and benchmark materials across operational temperatures (200, 300, 433 K) via DFT and experimental methods.

Sensors	Gas	τ (s)			Method
		200 K	300 K	τ433 K	
Mo_2NF_2	NO	1.9×10^{-3}	1.5×10^{-6}	1.9×10^{-8}	DFT
Mo_2NO_2	NO	1.9×10^{-3}	5.5×10^{-7}	9.2×10^{-9}	DFT
Ti_2NS_2 [22]	NO	1.7×10^{-2}	6.6×10^{-6}	5.2×10^{-8}	DFT
V_2NS_2 [22]	NO	1.1×10^{-5}	5.1×10^{-8}	1.8×10^{-9}	DFT
CrP [38]	NO	2.4×10^{-1}	8.8×10^{-4}	1.6×10^{-6}	DFT
$Ti_3C_2O_3$ [39]	NO	2.0×10^{-1}	7.2×10^{-4}	1.4×10^{-6}	DFT
Phosphorene [40]	NO	2.2×10^{-6}	1.6×10^{-8}	7.9×10^{-10}	DFT
$Pt/Cr\text{-}TiO_2/Pt$based [41]	NO_2	24	…	…	Experiment
$ZnO/ZnCo_2O_4$ [42]	H_2S	…	…	94	Experiment

candidates worthy of experimental validation with proper nanostructure engineering.

F. Transport properties of nanodevices constructed

As indicated in Table I, functionalized Mo_2NF_2 and Mo_2NO_2 sheets exhibit optimal adsorption energies and significant charge transfer for NO gas. This suggests a favorable balance between the desorption and adsorption of NO on these substrates, positioning them as promising candidates for gas-sensing applications. Upon adsorption, NO molecules interact with the substrate, altering its resistivity. This resistivity change can be detected as a variation in current under applied bias, analogous to functionalized materials like M_2CO_2 ($M=$ Sc, Ti, Zr, Hf), Mo_2CT_x, Nb_2CT_x, and Mo_2BT_2, which have also been predicted as potential gas sensors [21,38,43,44].

To qualitatively evaluate the detection sensitivity of Mo_2NF_2 and Mo_2NO_2 for NO, we constructed nanoscale sensor devices based on our DFT predictions. A schematic of the device is shown in Fig. 10(a). The device consists of three parts: the left semi-infinite electrode, the right semi-infinite electrode, and the central scattering region where the gas molecule absorbs.

In this study, the transport properties of the nanoscale devices were calculated using the nonequilibrium Green's function method implemented in the TRANSIESTA software package [38,45]. The Monkhorst-Pack k-point grids were set to $40 \times 4 \times 1$ for the electrodes and $1 \times 4 \times 1$ for the device. A 5×3 supercell obtained from structural relaxation was selected as the scattering region to compute transport properties. The scattering region was periodically extended to construct "pseudoelectrodes." Only the most stable NO-adsorption configuration within the scattering region was considered. The Landauer-Büttiker equation was used to estimate the current through the contact region [46,47]:

$$I(V_b) = G_0 \int_{\mu_L}^{\mu_R} T(E, V_b)[\delta(E-\mu_R) - \delta(E-\mu_L)]dE \tag{5}$$

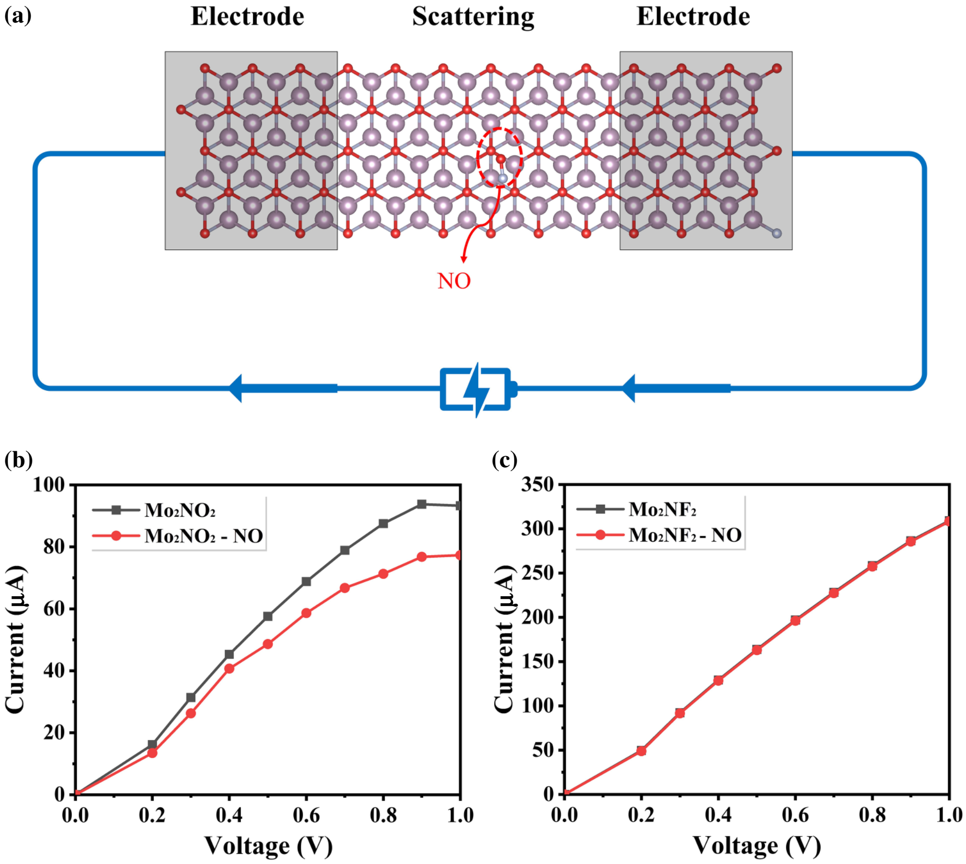

FIG. 10. (a) Schematic diagram of the nanodevice (using Mo_2NO_2 as an example) consists of three parts: the left semi-infinite electrode, the right semi-infinite electrode, and the gas-molecule scattering region. (b) Current-voltage (I-V) curves of pristine Mo_2NF_2 and Mo_2FO_2 under NO adsorption. (c) Current-voltage (I-V) curves of pristine Mo_2NO_2 and Mo_2NO_2 under NO adsorption.

where G_0 is the quantum conductance unit, and $T(E, V_\mathrm{b})$ represents the transmission probability of an electron with energy E under an applied bias voltage V_b. The potential difference between the left and right electrodes is given by $eV_\mathrm{b} = \mu_\mathrm{L} - \mu_\mathrm{R}$.

By solving the nonequilibrium Green's function, we analyzed the transport properties of the nanoscale device both before and after gas adsorption. The current-voltage (I-V) curves for the pristine scattering region and the NO-adsorbed scattering region are compared in Figs. 10(b) and 10(c). For the nanoscale device constructed with $\mathrm{Mo_2NF_2}$, the current exhibits a negligible change within the bias-voltage range of 0–1 V. In contrast, for the $\mathrm{Mo_2NO_2}$-based device, a significant current reduction is observed in the bias-voltage range of 0.6–0.9 V. Specifically, at bias voltages of 0.6 and 0.9 V, the current of the NO-adsorbed device measures 58.64 and 76.78 μA, respectively, representing reductions of 14.77% and 18.09% compared to the pristine device. This attenuation arises because the adsorbed molecules introduce localized potential barriers at the transport interface [48]. As evidenced by the differential charge density in Fig. 7(h), significant charge accumulation surrounds NO, intensifying electron scattering. Quantified via the Landauer-Büttiker equation [Eq. (5)]: $T(E, V_b)_\mathrm{ads} < T(E, V_b)_\mathrm{pristine}$ at $E \approx E_\mathrm{F}$. This suppression effect peaks within the 0.6–0.9 V bias range [Fig. 10(b)], directly driving current decay. Although charge transfer increases carrier concentration in the substrate, the adsorption energy primarily originates from the strengthening of the N—O bond due to electron depletion from NO's antibonding π^* orbitals. The limited interfacial interaction between NO and the $\mathrm{Mo_2NO_2}$ substrate implies that the enhancement in carrier concentration cannot compensate for the increased resistance induced by intensified electron scattering. This result indicates that $\mathrm{Mo_2NO_2}$ exhibits high sensitivity to NO. The adsorption of NO significantly reduces the current in monolayer $\mathrm{Mo_2NO_2}$, implying a substantial increase in resistance that can be directly measured experimentally. Therefore, $\mathrm{Mo_2NO_2}$ is a promising candidate material for NO-sensing applications.

G. Hydroxyl-dependent NO reactivity on mixed-terminated $\mathrm{Mo_2N}T_2$ surfaces

To elucidate the regulatory effects of the O-to-OH-group ratio on the structural stability and nitric-NO-adsorption behavior of $\mathrm{Mo_2N}T_2$ materials, systematic investigations were undertaken. Significantly, experimental findings revealed that $\mathrm{Mo_2N}T_2$ synthesized via ammonization of $\mathrm{Mo_2NO_2}$ possesses surfaces terminated by mixed O and OH functional groups. Consequently, computational models explicitly focusing on these coexisting terminations were employed.

First, employing a 3 × 3 supercell [Fig. 11], four distinct $\mathrm{Mo_2N}T_2$ configurations were constructed: $\mathrm{Mo_2NO_{1.89}(OH)_{0.11}}$-ST1, $\mathrm{Mo_2NO_{1.89}(OH)_{0.11}}$-ST2, $\mathrm{Mo_2NO_{0.89}(OH)_{1.11}}$-ST1, and $\mathrm{Mo_2NO_{0.89}(OH)_{1.11}}$-ST2. Notably, the $\mathrm{Mo_2NO_{1.89}(OH)_{0.11}}$ system models low hydroxyl coverage to isolate the impact of single OH groups, while the $\mathrm{Mo_2NO_{0.89}(OH)_{1.11}}$ system reflects a higher hydroxyl-to-oxygen ratio (∼8:10), designed to align with experimentally observed functional-group distributions. Analyses

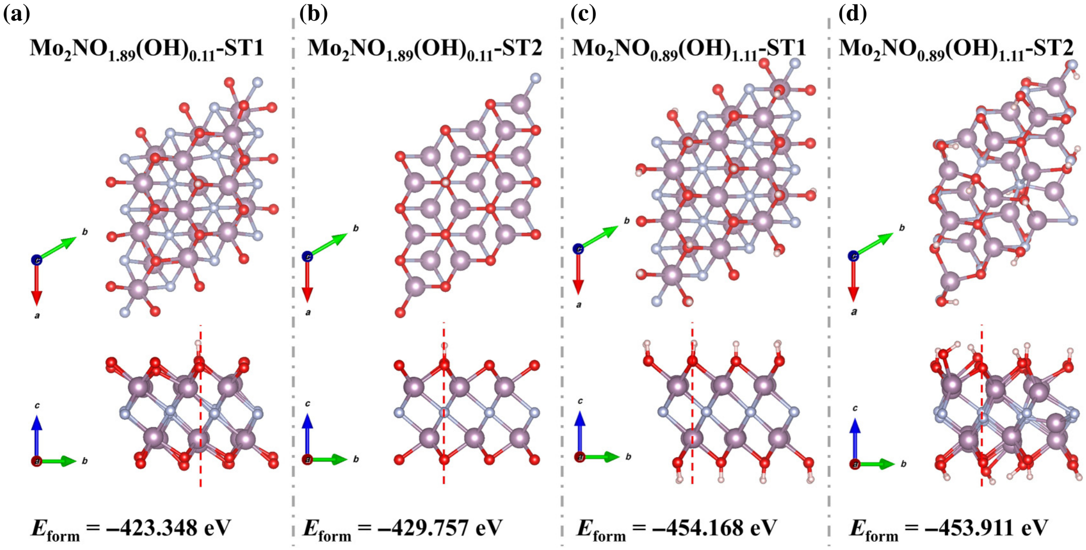

FIG. 11. Four distinct configurations of mixed-terminated $\mathrm{Mo_2N}T_2$ materials with varying hydroxyl group ratios: (a),(b) $\mathrm{Mo_2NO_{1.89}(OH)_{0.11}}$ system under low-OH concentration, revealing ST1 and ST2 conformations. (c),(d) $\mathrm{Mo_2NO_{0.89}(OH)_{1.11}}$ system under high-OH concentration, revealing ST1 and ST2.

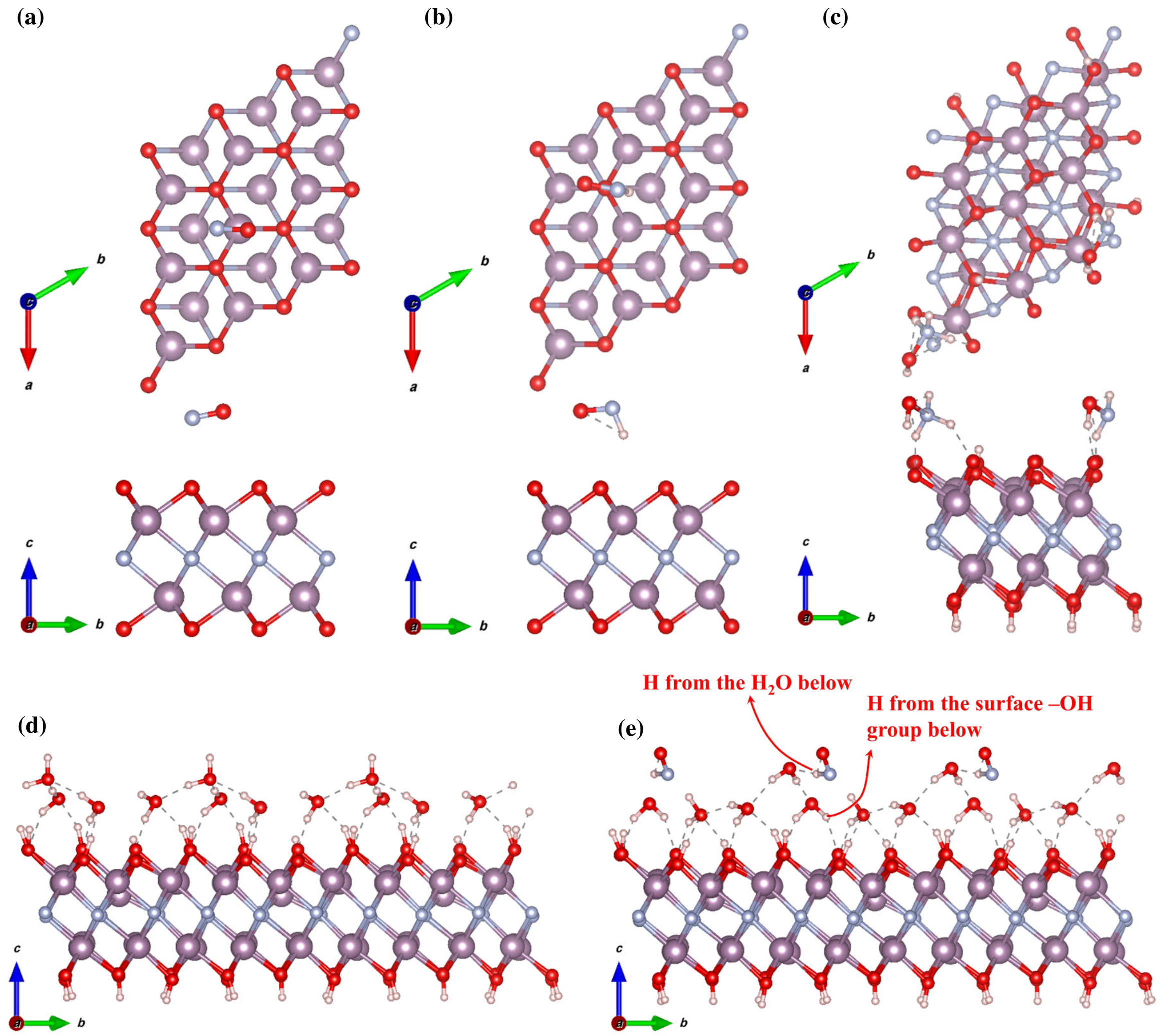

FIG. 12. NO-adsorption mechanisms on hydroxyl-functionalized surfaces. (a) Low-OH system [$Mo_2NO_{1.89}(OH)_{0.11}$]. (b) High-OH system [$Mo_2NO_{0.89}(OH)_{1.11}$]. (c) Water-passivated surface. (d) Surface configuration of $Mo_2NO_{0.89}(OH)_{1.11}$ passivated by water. (e) Stable configuration of NO adsorbed on the water-passivated surface.

revealed that, at low hydroxyl coverage, the ST2 configuration exhibited significantly lower formation energy relative to that of ST1. Conversely, under high hydroxyl coverage, the ST1 configuration dominated, highlighting the O:OH ratio as a critical determinant of ground-state structural stability.

Second, NO-adsorption studies (Fig. 12) demonstrated that the reaction pathway and products depended critically on the surface hydroxyl density. Crucially, in both regimes, NO instigates cleavage of O—H bonds within the material's surface OH groups. At low hydroxyl coverage, NO predominantly abstracts a single hydrogen atom from an OH group, yielding a stable O-N-H moiety. In contrast, at high hydroxyl coverage, NO reacts with more surface hydroxyl groups, resulting in the formation of hydroxylamine (H_2N-OH). This divergence underscores the concentration of surface hydroxyl groups as a pivotal factor modulating the NO-adsorption pathway and reaction outcome.

Finally, the influence of water passivation on NO-adsorption energetics was probed via configuration analysis (Fig. 12). Water passivation induced the formation of hydrogen-bonded networks on the surface. NO adsorption triggers a process where coordinated water molecules act as acceptors for hydrogen atoms abstracted from surface hydroxyl groups, thereby forming hydronium ions. Following this, the hydronium ions dissociate, yielding additional hydrogen atoms, which participate in reactions leading to nitroxyl (H-N-O) species formation. The computed adsorption energy for this passivated system was −1.010 eV. Crucially, while water passivation attenuated the reactivity (i.e., reduced the binding strength to −1.010 eV) compared to the strongly adsorptive and reactive nonpassivated system (−4.708 eV), irreversible chemical transformations occurred in both scenarios. The observed irreversible chemistry triggered by NO adsorption, even under passivation conditions, indicates that hydroxyl functional groups facilitate detrimental reactions. Consequently, these groups are likely detrimental to the efficacy of Mo_2N-based NO-sensing platforms, as passivation fails to sufficiently suppress the undesired chemical reactivity.

IV. CONCLUSION

This study establishes functionalized Mo_2NT_2 ($T = $H, O, F) MXenes as dual-functional platforms for toxic gas capture and sensing through systematic first-principles calculations. The pristine Mo_2N monolayer exhibits exceptional affinity for NO_x gases with adsorption energies up to −4.218 eV, demonstrating potential as an efficient capture agent. Surface-termination engineering critically modulates functionality: Mo_2NH_2 achieves selective NO_x capture, while Mo_2NO_2 emerges as an optimal NO sensor with moderate adsorption strength (−0.342 eV), substantial charge transfer (−0.197 e), and 14%–18% current reduction in nanodevices.

Beyond uniform surface terminations, the mixed-functionalized $Mo_2NO_x(OH)_y$ systems reveal hydroxyl-concentration-dependent reactivity—a pivotal advancement for practical applications. At low OH coverage, NO-triggered proton abstraction forms stable O-N-H moieties, whereas high OH content induces direct O-H cleavage, generating H_2N-OH. Although water passivation attenuates reaction strength ($E_{ads} = -1.010$ eV), irreversible chemical transformations persist, highlighting fundamental limitations of hydroxylated surfaces for reversible sensing. These findings underscore terminal-group control as the cornerstone for designing next-generation MXene-based gas-management systems, where precise surface-chemistry optimization is essential for balancing capture selectivity with sensing reversibility.

ACKNOWLEDGMENTS

This work was supported by the National Natural Science Foundation of China (Grants No. 62475145 and No. 12174246), the Shuguang Program of Shanghai Education Development Foundation, and the Shanghai Municipal Education Commission (Grant No. 22SG51).

The authors declare no competing financial interest.

DATA AVAILABILITY

The data that support the findings of this article are openly available [49].

[1] M. A. H. Khan, M. V. Rao, and Q. Li, Recent advances in electrochemical sensors for detecting toxic gases: NO_2, SO_2 and H_2S, Sensors **19**, 905 (2019).

[2] N. Yi, M. Shen, D. Erdely, and H. Cheng, Stretchable gas sensors for detecting biomarkers from humans and exposed environments, TrAC, Trends Anal. Chem. **133**, 116085 (2020).

[3] M. Khatib and H. Haick, Sensors for volatile organic compounds, ACS Nano **16**, 7080 (2022).

[4] J. M. Suh, W. Sohn, Y.-S. Shim, J.-S. Choi, Y. G. Song, T. L. Kim, J.-M. Jeon, K. C. Kwon, K. S. Choi, C.-Y. Kang, H.-G. Byun, and H. W. Jang, *p–p* heterojunction of nickel oxide-decorated cobalt oxide nanorods for enhanced sensitivity and selectivity toward volatile organic compounds, ACS Appl. Mater. Interfaces **10**, 1050 (2018).

[5] Y. Linghu and C. Wu, $1T'$-MoS_2, A promising candidate for sensing NO_x, J. Phys. Chem. C **123**, 10339 (2019).

[6] E. Lee and D.-J. Kim, Review—recent exploration of two-dimensional MXenes for gas sensing: From a theoretical to an experimental view, J. Electrochem. Soc. **167**, 037515 (2020).

[7] J. Li, X. Chen, X. Zhu, Y. Jiang, X. Chang, and S. Sun, Two-dimensional transition metal MXene-based gas sensors: A review, Chin. Chem. Lett. **35**, 108286 (2024).

[8] A. Sinha, Dhanjai, H. Zhao, Y. Huang, X. Lu, J. Chen, and R. Jain, MXene: An emerging material for sensing and biosensing, TrAC, Trends Anal. Chem. **105**, 424 (2018).

[9] B. Urasinska-Wojcik, T. A. Vincent, M. F. Chowdhury, and J. W. Gardner, Ultrasensitive WO_3 gas sensors for NO_2 detection in air and low oxygen environment, Sens. Actuators, B **239**, 1051 (2017).

[10] M. Kyselak, J. Vavra, K. Slavicek, D. Grenar, and L. Hudcova, Long distance military fiber-optic polarization sensor improved by an optical amplifier, Electronics **12**, 1740 (2023).

[11] T. Liang, Z. Dai, Y. Liu, X. Zhang, and H. Zeng, Suppression of Sn_2^+ and Lewis acidity in SnS_2/black phosphorus heterostructure for ppb-level room temperature NO_2 gas sensor, Sci. Bull. **66**, 2471 (2021).

[12] K. Deshmukh, T. Kovářík, and S. K. Khadheer Pasha, State of the art recent progress in two dimensional MXenes based gas sensors and biosensors: A comprehensive review, Coord. Chem. Rev. **424**, 213514 (2020).

[13] J.-J. Zhang and S. Dong, Superconductivity of monolayer Mo_2C: The key role of functional groups, J. Chem. Phys. **146**, 034705 (2017).

[14] M. Naguib, V. N. Mochalin, M. W. Barsoum, and Y. Gogotsi, 25th anniversary article: MXenes: A new family of two-dimensional materials, Adv. Mater. **26**, 992 (2014).

[15] E. Lee, A. VahidMohammadi, Y. S. Yoon, M. Beidaghi, and D.-J. Kim, Two-dimensional vanadium carbide MXene for gas sensors with ultrahigh sensitivity toward nonpolar gases, ACS Sens. **4**, 1603 (2019).

[16] L. Damptey, B. N. Jaato, C. S. Ribeiro, S. Varagnolo, N. P. Power, V. Selvaraj, D. Dodoo-Arhin, R. V. Kumar, S. P. Sreenilayam, D. Brabazon, V. Kumar Thakur, and S. Krishnamurthy, Surface functionalized MXenes for wastewater treatment—a comprehensive review, Glob. Chall. **6**, 2100120 (2022).

[17] X. Zhang, Z. Zhang, and Z. Zhou, MXene-based materials for electrochemical energy storage, J. Energy Chem. **27**, 73 (2018).

[18] X. Xie, S. Chen, W. Ding, Y. Nie, and Z. Wei, An extraordinarily stable catalyst: Pt NPs supported on two-dimensional $Ti_3C_2X_2$ ($X = $OH, F) nanosheets for oxygen reduction reaction, Chem. Commun. **49**, 10112 (2013).

[19] E. Lee, A. VahidMohammadi, B. C. Prorok, Y. S. Yoon, M. Beidaghi, and D.-J. Kim, Room temperature gas sensing of two-dimensional titanium carbide (MXene), ACS Appl. Mater. Interfaces **9**, 37184 (2017).

[20] P. Khakbaz, M. Moshayedi, S. Hajian, M. Soleimani, B. B. Narakathu, B. J. Bazuin, M. Pourfath, and M. Z. Atashbar, Titanium carbide MXene as NH_3 sensor: Realistic first-principles study, J. Phys. Chem. C **123**, 29794 (2019).

[21] B. Xiao, Y.-c. Li, X.-f. Yu, and J.-b. Cheng, MXenes: Reusable materials for NH_3 sensor or capturer by controlling the charge injection, Sens. Actuators, B **235**, 103 (2016).

[22] S. R. Naqvi, V. Shukla, N. K. Jena, W. Luo, and R. Ahuja, Exploring two-dimensional M_2NS_2 ($M = $Ti, V) MXenes based gas sensors for air pollutants, Appl. Mater. Today **19**, 100574 (2020).

[23] A. Shukla, G. Sharma, and S. Krishnamurty, Functionalized Mo_2BX_2 ($X = $H, OH, O) MBenes as a promising sensor, capturer and storage material for environmentally toxic gases: A case study of $1T$ and $2H$ phase, Appl. Surf. Sci. **615**, 156299 (2023).

[24] P. Urbankowski, B. Anasori, K. Hantanasirisakul, L. Yang, L. Zhang, B. Haines, S. J. May, S. J. L. Billinge, and Y. Gogotsi, 2D molybdenum and vanadium nitrides synthesized by ammoniation of 2D transition metal carbides (MXenes), Nanoscale **9**, 17722 (2017).

[25] V. Mehta, H. S. Saini, S. Srivastava, M. K. Kashyap, and K. Tankeshwar, Assessment of Mo_2N monolayer as Li-ion battery anodes with high cycling stability, Mater. Today Commun. **26**, 102100 (2021).

[26] J. Hafner, Materials simulations using VASP—a quantum perspective to materials science, Comput. Phys. Commun. **177**, 6 (2007).

[27] J. P. Perdew and Y. Wang, Accurate and simple analytic representation of the electron-gas correlation energy, Phys. Rev. B **45**, 13244 (1992).

[28] J. P. Perdew, K. Burke, and M. Ernzerhof, Generalized gradient approximation made simple, Phys. Rev. Lett. **77**, 3865 (1996).

[29] A. V. Krukau, O. A. Vydrov, A. F. Izmaylov, and G. E. Scuseria, Influence of the exchange screening parameter on the performance of screened hybrid functionals, J. Chem. Phys. **125**, 224106 (2006).

[30] S. Grimme, J. Antony, S. Ehrlich, and H. Krieg, A consistent and accurate *ab initio* parametrization of density functional dispersion correction (DFT-D) for the 94 elements H-Pu, J. Chem. Phys. **132**, 154104 (2010).

[31] R. Dronskowski and P. E. Bloechl, Crystal orbital Hamilton populations (COHP): Energy-resolved visualization of chemical bonding in solids based on density-functional calculations, J. Phys. Chem. **97**, 8617 (1993).

[32] Y. Yan, Y. Luo, Y. Li, Y. Zhang, P. Wu, J. Tang, X. Zhang, and S. Xiao, Transition metal (Au, Ag, Pt, Pd, Ni) doped MoS_2 as gas sensing materials for C_4F_7N leakage detection: A comparative study, Surf. Interfaces **44**, 103625 (2024).

[33] Z. S. Pereira, G. M. Faccin, and E. Z. da Silva, Strain-induced multigap superconductivity in electrene Mo_2N: A first principles study, Nanoscale **14**, 8594 (2022).

[34] See the Supplemental Material at http://link.aps.org/supplemental/10.1103/jst3-45bj for thermal stability analysis via AIMD simulations, phonon-dispersion spectra, gas-adsorption configurations, electronic structure analysis, and detailed adsorption parameters.

[35] S. Chen, S. Sun, B. Lian, Y. Ma, Y. Yan, and S. Hu, The adsorption and dissociation of H_2S on Cu(100) surface: A DTF study, Surf. Sci. **620**, 51 (2014).

[36] T. Usman, H.-j. Luo, Y. Zhang, X.-m. Tao, and M.-q. Tan, Adsorption and dissociation of H_2S on Rh(100) surface by first-principle study, Appl. Surf. Sci. **425**, 367 (2017).

[37] S. Satoh, H. Fujimoto, and H. Kobayashi, Theoretical study of NH_3 adsorption on Fe(110) and Fe(111) surfaces, J. Phys. Chem. B **110**, 4846 (2006).

[38] Z.-H. Yang, J.-H. Ren, T. Huang, W.-Q. Huang, W.-Y. Hu, and G.-F. Huang, Two-dimensional chromium phosphorus monolayer based gas sensors to detect NO_x: A first-principles study, Results Phys. **32**, 105100 (2022).

[39] M. Wu, M. He, Q. Hu, Q. Wu, G. Sun, L. Xie, Z. Zhang, Z. Zhu, and A. Zhou, Ti_3C_2 MXene-based sensors with high selectivity for NH_3 detection at room temperature, ACS Sens. **4**, 2763 (2019).

[40] S. Lei, R. Gao, X. Sun, S. Guo, H. Yu, N. Wan, F. Xu, and J. Chen, Nitrogen-based gas molecule adsorption of monolayer phosphorene under metal functionalization, Sci. Rep. **9**, 12498 (2019).

[41] A. A. Haidry, Q. Fatima, A. Mehmood, A. Shahzad, Y. Ji, and B. Saruhan, Adsorption kinetics of NO_2 gas on Pt/Cr-TiO_2/Pt-based sensors, Chemosensors **10**, 11 (2022).

[42] T. Xu, J. Zhao, F. Zhao, W. Cong, and G. Wang, Synthesis of ZnO/$ZnCo_2O_4$ hollow tube clusters by a template method for high-sensitive H_2S sensor, Sens. Actuators, B **394**, 134338 (2023).

[43] F. Pan, B. Sun, Z. Tang, and S. Zhu, A fast response cataluminescence ether gas sensor based on GO/$Mo_2TiC_2T_x$ at low working temperature, RSC Adv. **12**, 8361 (2022).

[44] K. Wang, J. Li, J. Li, J. Guo, H. Li, S. Li, R. Tu, Y. Liu, and C. Zhang, F-functionalized Sc_2C monolayer as a high sensitivity nitrogen-containing gases sensor, Mater. Sci. Semicond. Process. **182**, 108709 (2024).

[45] M.-Q. Cheng, Q. Chen, K. Yang, W.-Q. Huang, W.-Y. Hu, and G.-F. Huang, Penta-graphene as a potential gas sensor for NO_x detection, Nanoscale Res. Lett. **14**, 306 (2019).

[46] Z. Wang, R. Zhang, Z. Liu, X. Wei, M. Zhao, X. Zhang, Y. Yong, H. Cui, and X. Li, C_6N_7 monolayer as an innovative sensor and scavenger for NO, H_2S and SO_2: A first-principles study, Surf. Interfaces **39**, 102971 (2023).

[47] E. Salih and A. I. Ayesh, DFT investigation of H_2S adsorption on graphene nanosheets and nanoribbons: Comparative study, Superlattices Microstruct. **146**, 106650 (2020).

[48] K. Zhao, Y. Shi, M. Cui, B. Tang, C. Zheng, Q. Chen, and Y. Hu, Flexible resistive gas sensor based on molybdenum disulfide-modified polypyrrole for trace NO_2 detection, Polymers **16**, 1940 (2024).

[49] Zenodo, https://doi.org.10.5281/zenodo.17120437 (2025).